# Intraseasonal Variability in the South Equatorial Current of the East Indian Ocean

MING FENG AND SUSAN WIJFFELS

*Division of Marine Research, Commonwealth Scientific and Industrial Research Organisation, Hobart, Tasmania, Australia*

(Manuscript received 27 April 2000, in final form 27 June 2001)

ABSTRACT

Satellite altimeter data reveal that the strongest intraseasonal variability in the southeast Indian Ocean occurs in the South Equatorial Current (SEC) during the second half of the year. The length scale of the variability is 100–150 km, with a westward phase speed of 15–19 cm $s^{-1}$ and dominant periods between 40 and 80 days. A continuously stratified quasigeostrophic model is solved to analyze the baroclinic stability of the climatological SEC. Large growth rate of the instability waves (with *e*-folding timescale of less than 50 days) can be found east of the active region of intraseasonal variability during the July–September season, when the SEC and the Pacific to Indian Ocean throughflow are at their strongest. Geostrophic current shear in the upper 200-m ocean is crucial for the growth of the instability. The results suggest that the baroclinic instability draws most of its energy from the available potential energy associated with the throughflow, and, to a lesser degree, by local Ekman pumping. The predicted characteristics of the most unstable mode are consistent with both altimeter and profiling float observations. From all the available evidence, baroclinic instability seems to be the main cause of intraseasonal variability in the SEC. However, more field observations are necessary to properly address the possibility of combined barotropic/baroclinic instability.

## 1. Introduction

The Pacific to Indian Ocean throughflow removes mass and heat from the western Pacific warm pool and affects the thermohaline circulation and air–sea heat exchange patterns of the global ocean (Gordon 1986; Broecker 1991; Hirst and Godfrey 1993; Godfrey 1996; Schneider and Barnett 1997; Schiller et al. 1998). The upper ocean throughflow volume transport is estimated to be 5–10 Sv (Sv $\equiv 10^6$ $m^3$ $s^{-1}$) with an annual variability of about 5 Sv. Maximum flow into the Indian Ocean occurs during the southeast monsoon from July to September as in observations (Meyers et al. 1995) and model results (Potemra 1999). The Indian Ocean circulation is not only forced by intense annually reversing monsoonal winds (Tomczak and Godfrey 1994), but also influenced by the throughflow variability.

The throughflow enters the east Indian Ocean through a series of straits along the Indonesian archipelago and the northwest coast of Australia (Lukas et al. 1996; Wijffels et al. 1996) (Fig. 1). In this region, the South Equatorial Current (SEC) flows westward, carrying low salinity throughflow water (34.2–34.6 psu; Bray et al. 1997). The geostrophic component of the SEC is also strongest from July to September (Meyers et al. 1995). The eastward-flowing shallow Eastern Gyral Current partly recirculates in the SEC and partly feeds the southward Leeuwin Current along the west coast of Australia. The South Java Current is an eastward flow observed semiannually near the Sumatra–Java coast (Quadfasel and Cresswell 1992; Sprintall et al. 2000), and is forced by equatorial Indian Ocean winds.

From satellite altimetric surface height fields and sea level data from Christmas Island (10.5°S, 106°E), Bray et al. (1997) detected energetic eddies and meanders with 60-day timescale in the SEC south of Java. The observed intraseasonal signals were comparable in magnitude to seasonal and interannual variability and they accounted for much of the variation in water mass properties between repeat hydrographic cruises (Wijffels et al. 2001). This signal is also found in the drifter data of Quadfasel et al. (1996) and in the Semtner and Chervin (1992) model forced by climatological monthly mean wind stress (Ponte and Gutzler 1992). However, it was not reproduced in a 1½ layer reduced gravity model (Qiu et al. 1999), which does not permit the vertical reversal of meridional potential vorticity gradient. Hence, Qiu et al. speculated that this SEC variability is due to baroclinic instability.

Intraseasonal variability also occurs at the Pacific entrance of the throughflow (Watanabe et al. 1997; Kashino et al. 1999; Qiu et al. 1999), within the Indonesian seas [forced by atmospheric Madden–Julian oscillation (Madden and Julian 1994; Susanto et al. 2000)], and along the Sumatra–Java coast to Timor Passage [forced by local or Indian Ocean equatorial winds (Molcard et

*Corresponding author address:* Ming Feng, CSIRO Division of Marine Research, Castray Esplanade (GPO Box 1538), Hobart, Tasmania 7001, Australia.
E-mail: ming.feng@csiro.au

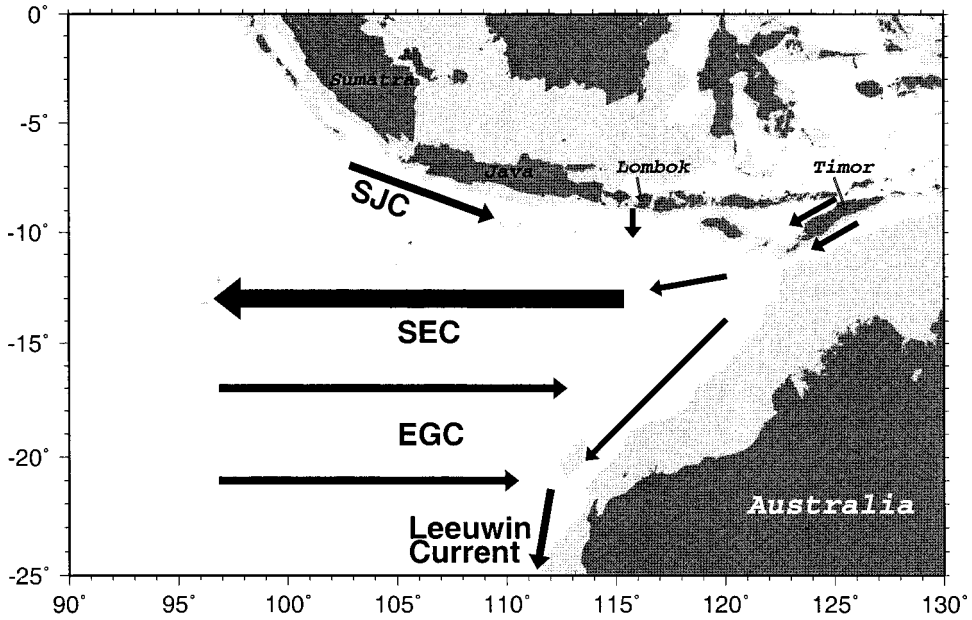


FIG. 1. The surface current structure in the east Indian Ocean. SEC: South Equatorial Current; EGC: Eastern. Gyral Current; SJC: South Java Current. The other arrows denote the flow directions of the Indonesian Throughflow. The light shading denotes the 1000-m isobath.

al. 1994, 1996; Arief and Murray 1996; Chong et al. 2000)]. In this study, we argue that the intraseasonal variability in the SEC is not a direct response to these mainly coastally trapped signals, but is indeed locally generated in the SEC through an instability process.

Eddy energetics diagnosed from satellite altimeter data suggests baroclinic instability to be the primary source of eddy energy over most of the World Ocean (Stammer 1997). Meridional eddy heat transport was found to be important in the western boundary currents, the Southern Ocean, and the tropical oceans (Stammer 1998). Available in situ mooring data are inadequate to confirm the altimetric results except in the Gulf Stream, the Kuroshio, and a small portion of the Southern Ocean (Wunsch 1999). The eddies in the SEC in the east Indian Ocean likely redistribute the throughflow's mass, heat, and freshwater fluxes along other related tracers such as carbon and potential vorticity. The throughflow heat transport is believed to be partly responsible for suppressing the cooling effect of wind-driven upwelling along the Sumatra–Java coast (Qu et al. 1994; Murtugudde et al. 1998), where interannual variability of the sea surface temperature is related to Australian rainfall patterns (Nicholls 1989), the evolution of ENSO (Meehl 1993), and Indian Ocean dipole events (Webster et al. 1999). Numerical model studies show that the throughflow structure and heat transport are sensitive to the choices of horizontal and vertical eddy transfer parameterizations (Murtugudde et al. 1998; Schiller et al. 1998). A detailed understanding of the eddy structure in the SEC, in which the throughflow is embedded, will allow a better assessment of their importance in affecting heat fluxes, as well as the mean circulation.

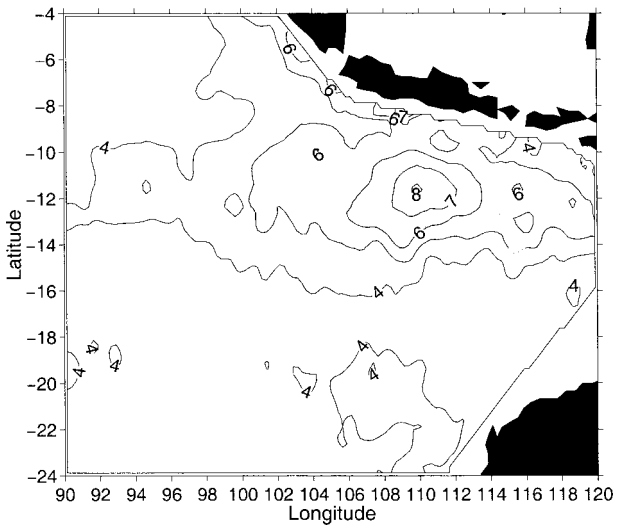


FIG. 2. Standard deviation of sea level anomaly from the 100-day high-pass filtered altimeter data. The shaded region denotes standard deviations larger than 5 cm.

Organization of this paper is as follows: in section 2, the data used in the study are described; in section 3, the intraseasonal variability in the SEC is characterized with altimeter data; in section 4, the cause of the intraseasonal variability is studied and a quasigeostrophic model is used to assess the baroclinic stability of the SEC; in section 5, the vertical structure of the predicted

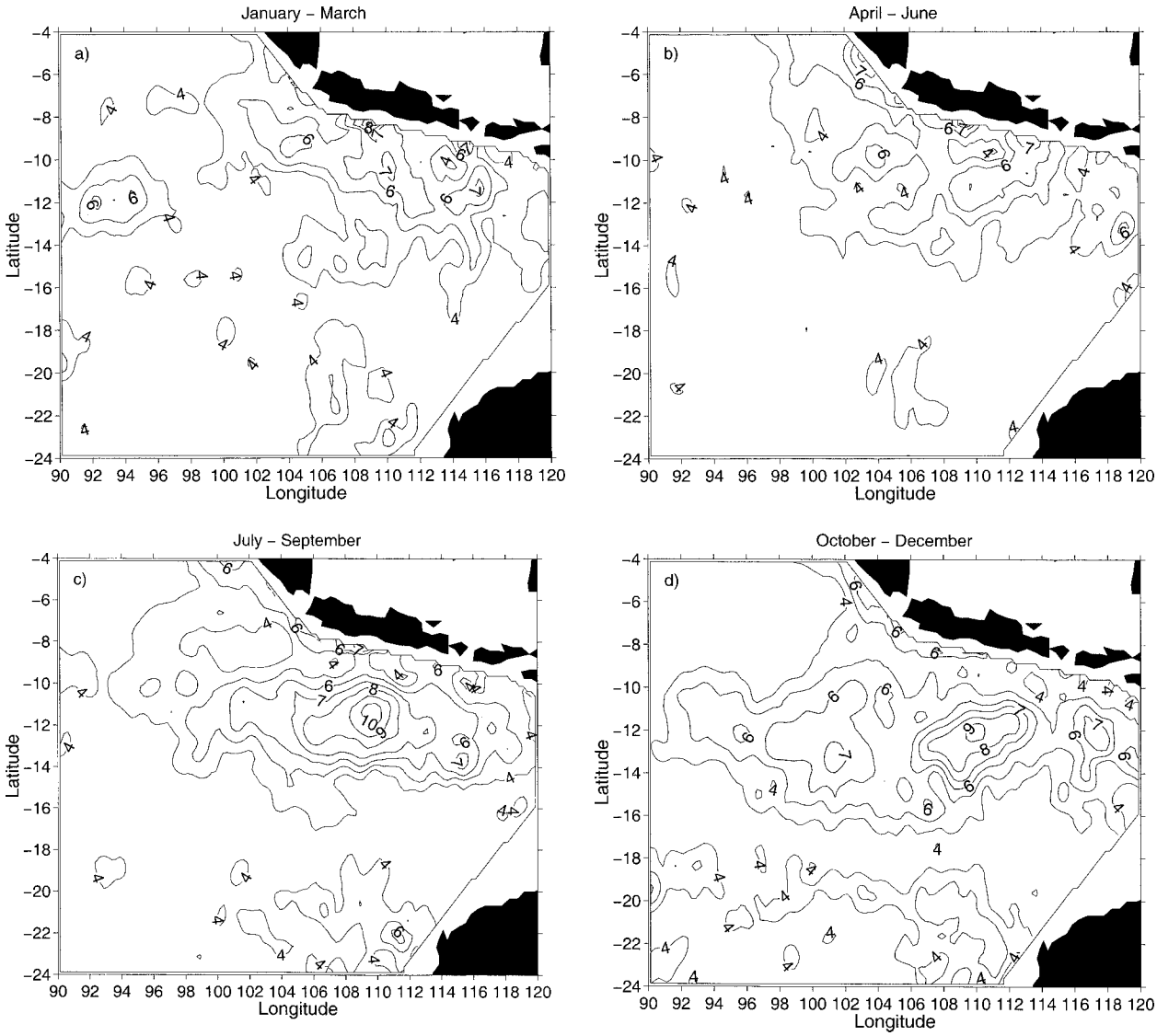


FIG. 3. Same as Fig. 2 except for standard deviations of sea level anomaly during the four seasons: (a) Jan–Mar; (b) Apr–Jun; (c) Jul–Sep; (d) Oct–Dec.

unstable wave is analyzed and compared with observations; in section 6, we analyze the available potential energy budget related to the baroclinic instability; in section 7, the effects of the instability on heat fluxes and the large-scale circulation are discussed; and finally, in section 8, we summarize the results.

## 2. Data

We use the gridded altimeter sea level anomaly from the first six years of the combined TOPEX/Poseidon and *ERS-1*/*ERS-2* missions (October 1992 to the end of 1998), obtained from Collecte, Localisation, Satellites (CLS) Space Oceanography Division. The data were gridded every 10 days with a 0.25° spatial resolution (Le Traon et al. 1998). Regions where water depths are shallower than 1000 m are removed from this analysis to avoid tidal alias.

Both seasonal and monthly one-degree gridded temperature and salinity climatologies are used (Levitus et al. 1994; Levitus and Boyer 1994). Wind stress data are from the National Centers for Environmental Prediction (NCEP) reanalyzed global meteorological dataset, which has a grid spacing of (about) 1.9° of latitude by 1.875° of longitude. Daily wind stress data during the altimeter observation time period are used. CTD temperature and salinity data from a World Ocean Circulation Experiment (WOCE) hydrographic section along 12°S during September 1995 are also used in this study [for detailed cruise information, see Wijffels et al. (1996)].

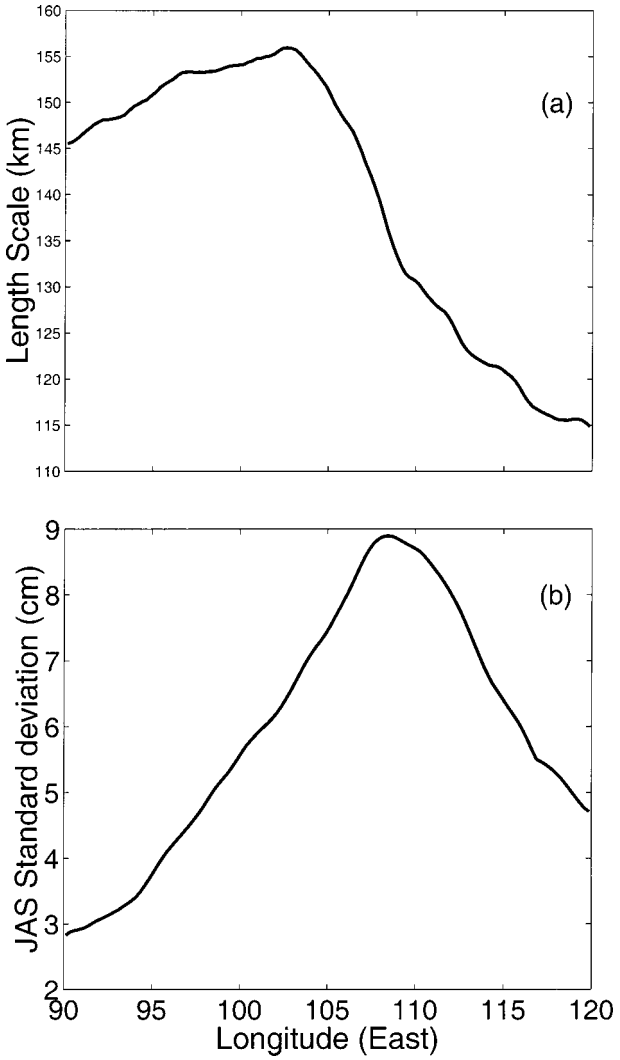


FIG. 4. (a) Horizontal length scale and (b) standard deviation (Jul–Sep season) of the 100-day high-pass filtered altimeter data along 12°S. A 6-degree moving zonal average is used to smooth the results.

Supported by a special executive grant of CSIRO and as part of the international Argo program, PALACE (Profiling Autonomous Lagrangian Circulation Explorer) floats manufactured by the Webb Research Corporation were deployed in October 1999 in the east Indian Ocean including the SEC region. The floats drifted at 2000 m, and surfaced every 10 days to measure and deliver temperature and salinity profile data. One float (21071), parked near 11–12°S, 109°E, sampled the strong intraseasonal signals in the SEC during June–September 2000. The salinity sensor of this float was calibrated using nearby deep WOCE CTD data. Due to lack of buoyancy produced at depth, the float was unable to surface normally so that the measurements stop at about 100 m. Data in the upper 500 m are used in this study.

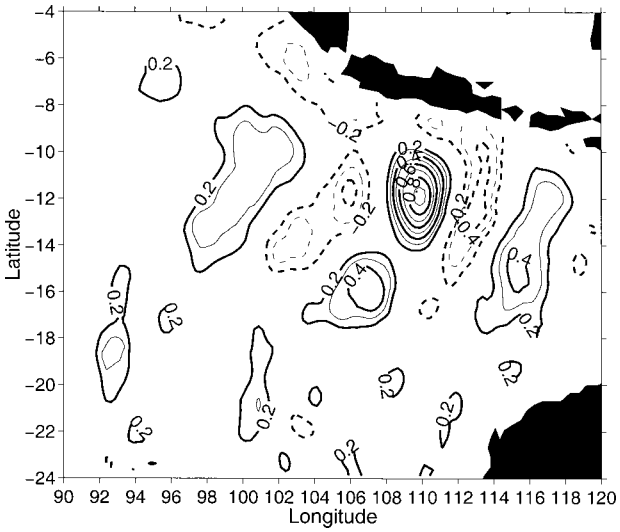


FIG. 5. Zero-lag correlation of sea level anomaly with that at 12°S, 110°E.

## 3. Altimeter observations

The standard deviation of the 100-day high-passed altimeter sea level anomaly shows two regions of large magnitude (Fig. 2): one is coastally trapped along the southern Sumatra–Java coast, the other is offshore centered at 11°–12°S, 110°E, extending in the east–west direction from 100° to 120°E. South of 18°S, there is an isolated region with sea level standard deviation higher than 4 cm, which is probably related to the Leeuwin Current variability and is not examined in the present study.

Intraseasonal coastal Kelvin waves along the Sumatra–Java coast are generated by Indian Ocean winds (Arief and Murray 1996). They are stronger in January–June (Figs. 3a,b), consistent with 3-yr shallow pressure-gauge records at the Lombok Strait (Chong et al. 2000). The energy in the coastal wave guide drops east of Lombok Strait, suggesting that part of the intraseasonal Kelvin wave signal propagates into the Indonesian seas through Lombok Strait, as in models (Qiu et al. 1999) and shallow pressure gauge results (Sprintall et al. 1999, 2000). The interior ocean signals along 10°S during January–June might be due to Kelvin wave reflection, which needs further study.

Intraseasonal variability in the SEC region is weak during the first half of the year, but is strong during July–September, with maximum standard deviation of 10 cm near 110°E (Fig. 3c). The magnitude decreases slightly during October–December, but the variability extends zonally (Fig. 3d). The different seasonal modulation of the intraseasonal variability in the SEC (with highest energy during second half of the year) suggests that it is distinct from the signals along the Sumatra–Java coast (which are strongest during the first half of the year).

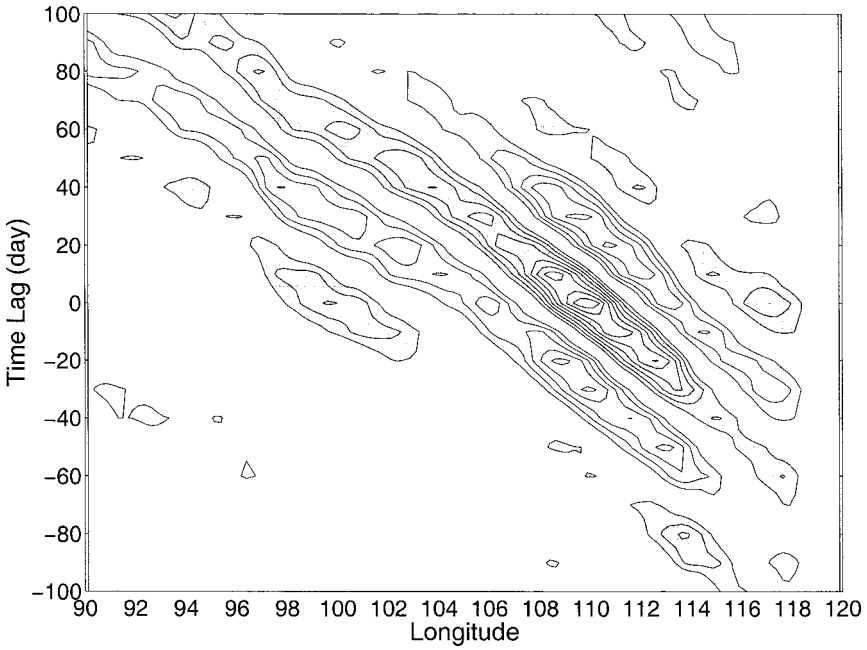


FIG. 6. Time–longitude lag-correlation diagram of sea level anomaly along 12°S centered at 110°E. The contours start from 0.2 with 0.1 increment and shaded areas denote positive correlations.

The dominant length scale of the variability is calculated using spatial correlation of 100-day high-passed altimeter data. Centered at each grid point, altimeter data from 10° strips are used to calculate the average zonal and meridional length scales for the 6-yr dataset. The spatial scale along 12°S is about 150 km west of 106°E (Fig. 4a), similar to length scales derived from the alongtrack TOPEX/Poseidon altimeter data using the same correlation method (Stammer 1997). In addition, we find a general decrease of spatial scales east of 106°E that is not resolved by Stammer's calculation. Near 108°–110°E, where the energy is highest during July–September (Fig. 4b), the scale is between 120–130 km, slightly larger than the Rossby radius of 90 km of the first baroclinic mode calculated from the hydrographic climatology. Note that the minimum length scale estimated from the gridded data is dictated by its mapping decorrelation scale, which is about 250 km at 12°S (Le Traon et al. 1998) and barely resolves the above scales.

Cross-correlation (zero-lag) of sea level anomaly across the region with that at the location of peak variability (12°S, 110°E) shows pronounced zonal banding (Fig. 5), indicating east–west propagation with a slight northwestward trend. The wavelength, indicated by distance to the secondary correlation maxima, also increases westward from approximately 600 km (100 km length scale) east of 100°E, slightly smaller than results from Fig. 4, to about 900 km (150-km length scale) to the west. The time–longitude lag correlation of sea level anomaly along 12°S, centered at 110°E (Fig. 6), reveals a westward phase speed of about 15 and 19 cm $s^{-1}$ to the east and west of 110°E, respectively. This compares to the first-mode baroclinic Rossby wave phase speed $\beta c^2/f^2$ of 19 cm $s^{-1}$, where $c = 2.8$ m $s^{-1}$ is the gravity wave phase speed, $f$ is the Coriolis parameter, and $\beta$ is its meridional gradient (see appendix). Thus, the phase speed west of 110°E is consistent with a free Rossby wave.

A wavelet analysis (Lau and Weng 1995) of the sea level anomaly (here 200-day high-passed data are used to include semiannual energy) shows that, while stronger intraseasonal variability along 12°E occurs during the second half of the year, there are substantial interannual variations in both strength and period. Peak amplitudes range from 9 to 16 cm and the dominant periods vary from 40 to 80 days (Fig. 7a). The SEC is anomalously stronger during 1994 and 1997, the Indian Ocean dipole years (Feng et al. 2001), which is coincident with the intense intraseasonal energy in the SEC (Fig. 7a). The variability near the Sumatra–Java coast is dominantly semiannual (Fig. 7b). While there are also interannual variations in the intraseasonal band, they do not appear to be related to the variability found along 12°S. Lagged correlations also show that the variability in the coastal wave guide does not significantly correlate or lead that at 12°S, 110°E (not shown).

In summary, the intraseasonal variability in the SEC has a time period of 40–80 days, a length scale of 100–150 km, and a westward phase speed of 15–19 cm $s^{-1}$. Largest amplitudes occur from July–September, and the

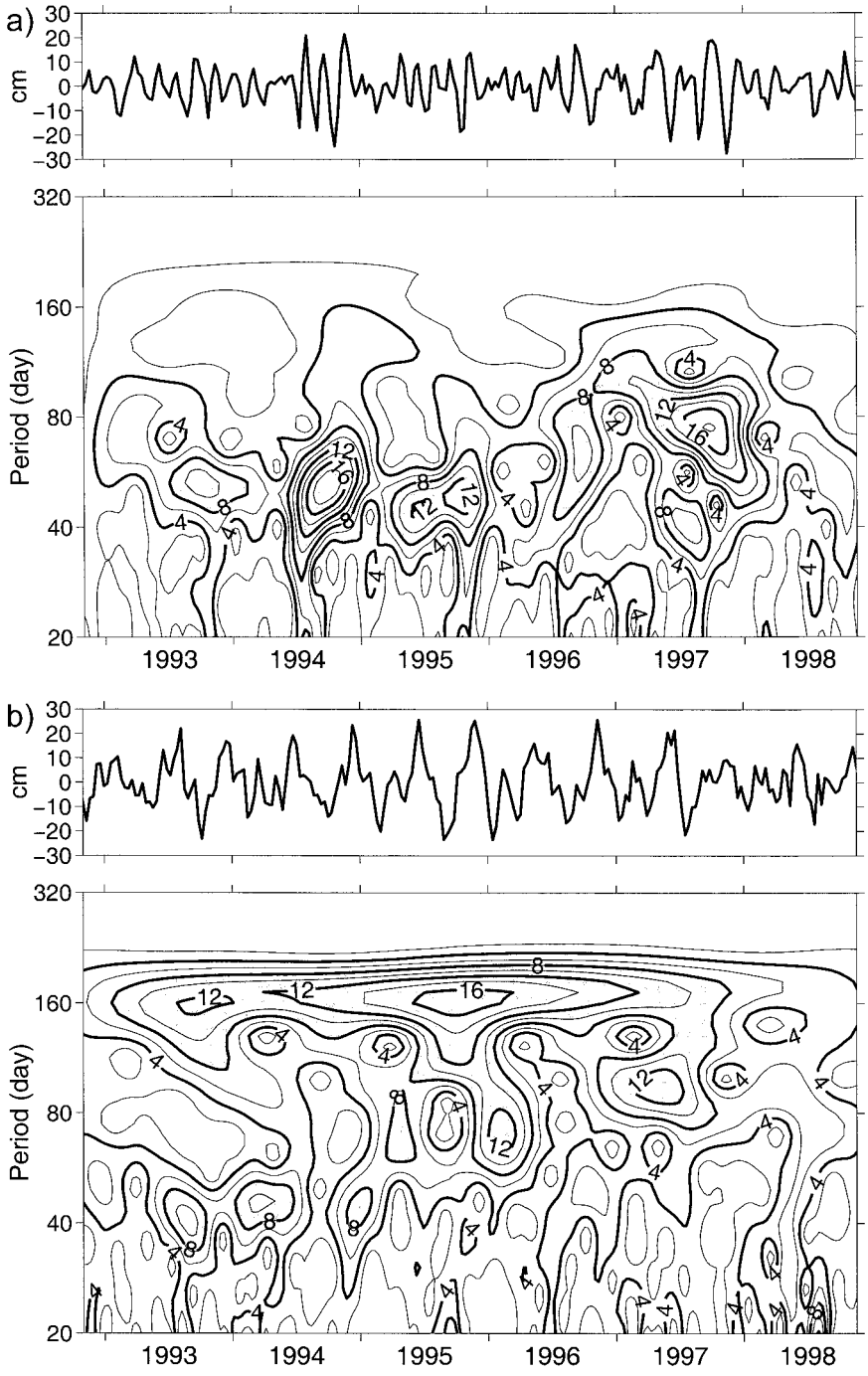


FIG. 7. Time series (upper panel) and wavelet analysis amplitude (lower panel) of sea level anomaly at (a) 12°S, 110°E and (b) 8.5°S, 108°E. The shaded areas denote amplitudes larger than 8 cm.

signal is not correlated with activity in the Java/Sumatra coastal wave guide.

## 4. Origin of intraseasonal energy in the SEC

The two most likely causes of intraseasonal energy in the open ocean are direct wind forcing and mean flow instability. The intraseasonal signal in the SEC is not correlated with that along the Sumatra–Java coast, so remote driving by equatorial Indian Ocean intraseasonal wind forcing can be excluded. We also find no strong intraseasonal variance along the low-latitude northwest Australian shelf break, suggesting that remote forcing of the SEC via Pacific intraseasonal winds is also not likely.

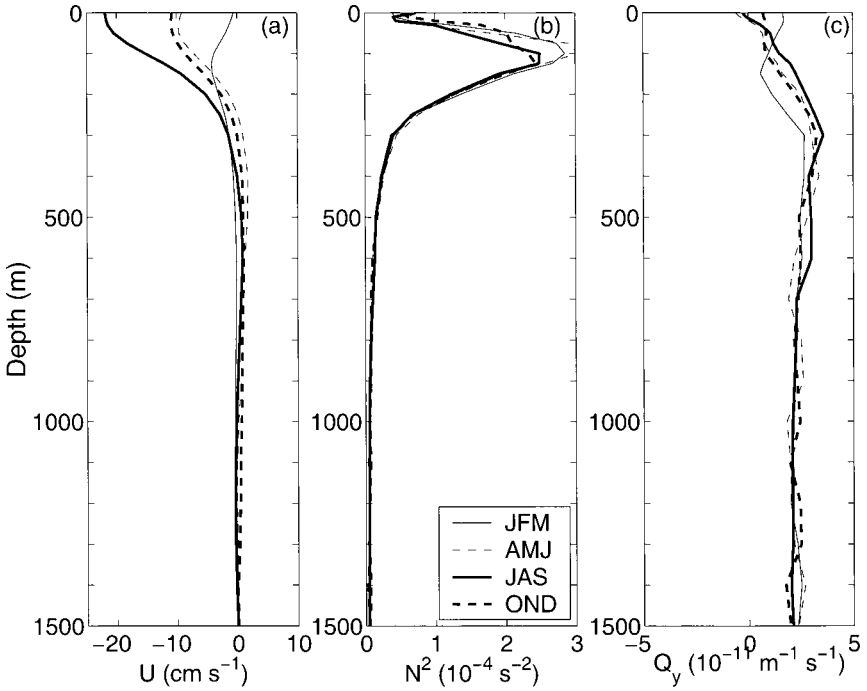


FIG. 8. (a) Geostrophic zonal velocity, (b) buoyancy frequency squared, and (c) meridional gradient of potential vorticity from seasonal climatology averaged between 10.5° and 12.5°S at 113.5°E.

The local intraseasonal Ekman pumping rate calculated from the 100-day high-pass filtered NCEP wind stress product (not shown) has a standard deviation of only 1.5–2 $\times$ $10^{-6}$ m s$^{-1}$ along 12°S and without significant seasonal variation. This forcing could generate only a 1-cm sea level change over 30 days using a reduced gravity of 0.02 m s$^{-2}$. Thus, even considering a 50% uncertainty in the NCEP wind stress, the direct wind-driven effect can be excluded as a primary generation mechanism.

To examine the stability of the SEC, we utilize the zonal geostrophic velocity, $\overline{U}$, calculated from the seasonal hydrographic climatology. In the SEC region, $\partial^2\overline{U}/\partial y^2$ has a magnitude of 3 $\times$ $10^{-12}$ m$^{-1}$ s$^{-1}$, which is much smaller than $\beta$. Thus, a necessary condition (Gill 1982) for barotropic instability is not satisfied. Philander (1978) suggested that a barotropic instability analysis should use the ''undisturbed mean state,'' which is not possible here due to the lack of long-term direct current measurements in this region. Along with the likelihood that the lateral smoothing required to produce the seasonal hydrographic climatology has reduced $\partial^2\overline{U}/\partial y^2$, we find that we do not have adequate data to address the possibility that barotropic instability may play some role in this region. While mean flow instabilities are typically mixed, the available data only allow a theoretical examination of the potential for baroclinic instability, which we pursue below.

Following Gill et al. (1974), we explore the baroclinic stability of the SEC using a linear continuously stratified quasigeostrophic model based on the climatological hydrographic fields (see appendix for details). At the suggestion of one reviewer, we also added the $\partial^2\overline{U}/\partial y^2$ term to the background meridional potential vorticity gradient (Ripa 1991), but with $\overline{U}$ in a simplified parabolic form.

Comparing the velocity structure during different seasons, we find that the SEC has the strongest vertical shear during July–September (Fig. 8a), with mean flow Richardson number Ri of 2000 averaged over the upper 500 m, where most of the energy conversion occurs (see below). In an Eady model, the growth rate of the baroclinic instability is $f/\mathrm{Ri}^{1/2}$ (Visbeck et al. 1997), which equals 1/20 day$^{-1}$ during the July–September season. Compared to conditions in July–September, Ri is almost an order of magnitude larger during other seasons, when the mean flow is more stable. The weaker seasonal stratification during the second half of the year also facilitates the instability process (Fig. 8b).

The necessary conditions for the baroclinic instability are satisfied for most seasons (Fig. 8c); that is, either there is a zero crossing in the potential vorticity gradient (satisfying Gill's first condition of instability), or the potential vorticity gradient has a different sign to the velocity shear at sea surface (satisfying Gill's second condition of instability). However, by solving the quasigeostrophic model (see appendix), the July–September season was found to be the only one during which a baroclinic instability wave can grow intraseasonally (high growth rates are found only in July and August

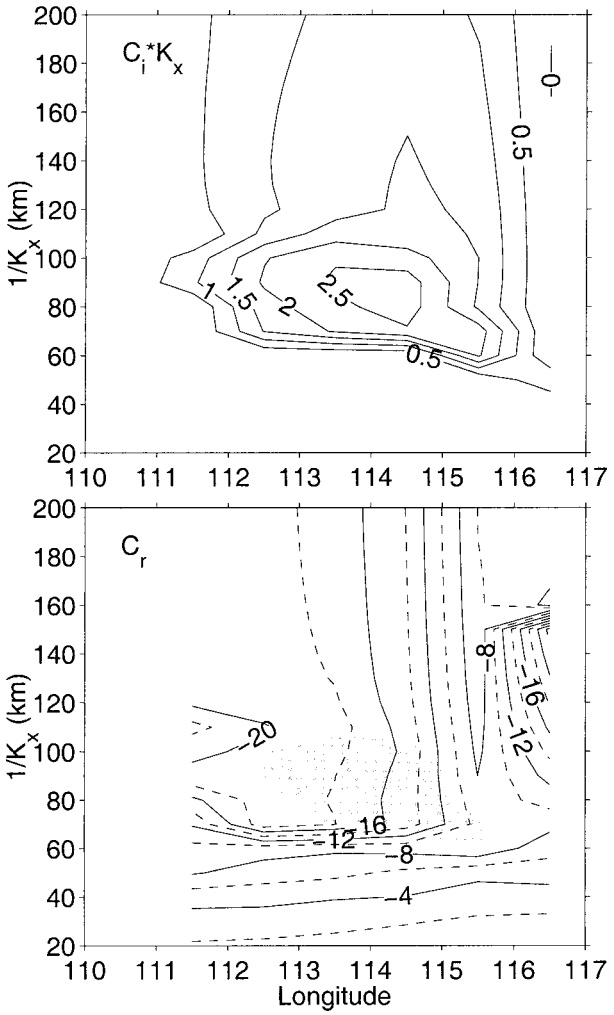


FIG. 9. Growth rate ($10^{-2}$ day$^{-1}$) and phase speed (cm s$^{-1}$) from the instability analysis of the seasonal climatology data averaged between 10.5° and 12.5°S during Jul–Sep. The shading in the lower panel denotes growth rates larger than $2 \times 10^{-2}$ day$^{-1}$. The growth rates outside the plotted longitudes are small and the phase speeds are noisy, so that they are omitted from the plot.

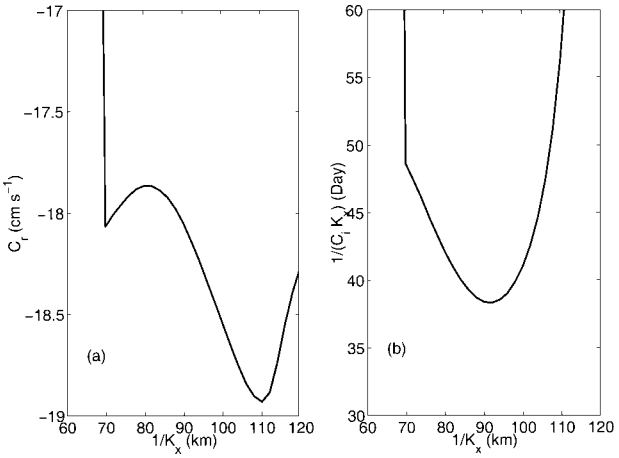


FIG. 10. (a) Phase speed and (b) inverse growth rate from the instability analysis of the seasonal climatology data averaged between 10.5° and 12.5°S at 113.5°E during Jul–Sep.

when calculated using the monthly climatology), with *e*-folding timescales shorter than 50 days. Similar results are found when we use a higher spatial resolution upper-ocean thermal climatology for the background state. Hence, we focus here on analyzing results for the July–September season.

In July–September, the longitudinal distribution of the eddy growth rate in the SEC was calculated for wavenumbers from 1/20 to 1/200 km$^{-1}$ (Fig. 9). Positive growth rates occur in all longitudes. Growth rates larger than 0.02 day$^{-1}$ are needed for the waves to grow intraseasonally. We find such growth rates between 112°–116°E where the observed intraseasonal energy increases westward (Fig. 4). The highest growth rate corresponds to wavenumbers between 1/100 and 1/70 km$^{-1}$. The deduced phase speed is smooth in the domain where the growth rate is high (Fig. 9) but is noisy where the growth rate is low, and so is omitted from the figure. The phase speeds of the most unstable waves show a westward increase from 9 to 19 cm s$^{-1}$ between 116° and 112°E with corresponding periods between 40 and 60 days. Recall that the observations showed a phase speed near 15 cm s$^{-1}$ east of 110°E. Note that the phase speed and the derived wave period from the eigenvalue problem is dependent on the reference depth of the geostrophic velocity, while the growth rate and wavenumber are not (Ripa 1991).

The unstable wave is only slightly dispersive from the phase speed/wavenumber relationship (Fig. 10). West of the region of active instability (116°–111°E), we find from the altimeter data that the phase speeds correspond to that of a free wave. Thus, we would argue that the intraseasonal energy along 12°S during October–December (Fig. 3d) is simply due to the zonal propagation of the weakly dispersive waves generated during the preceding July–September.

## 5. Subsurface structure

From the potential density data along 12°S (Fig. 11) and altimeter maps, the September 1995 WOCE section (IR6) cut through several large meanders found in the SEC. Maximum density anomalies of 0.8–1 kg m$^{-3}$ occur between 100–150 m in the upper pycnocline with associated temperature anomalies of 3°C and salinity anomalies of 0.15 psu (not shown). These are consistent with PALACE float observations within the SEC (Fig. 12), which show that the potential density anomaly grows from 0.5 kg m$^{-3}$ in June 2000 to nearly 1 kg m$^{-3}$ at the end of August (Fig. 12), with related temperature and salinity anomalies of 3°C and 0.2 psu (not shown).

To extract the average wave structure from the float data we fit the potential density variations with a sine wave of 60-day period at each depth to determine the

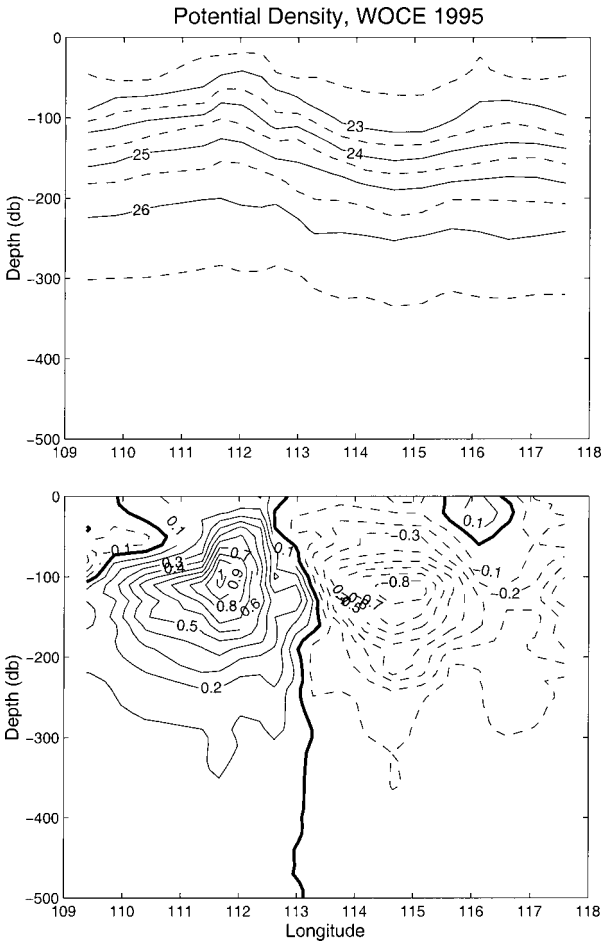


FIG. 11. Potential density $\sigma_\theta$ (upper panel) and its anomaly relative to a zonal average (lower panel) along a 12°S WOCE section during Sep 1995. The unit is kg m$^{-3}$.

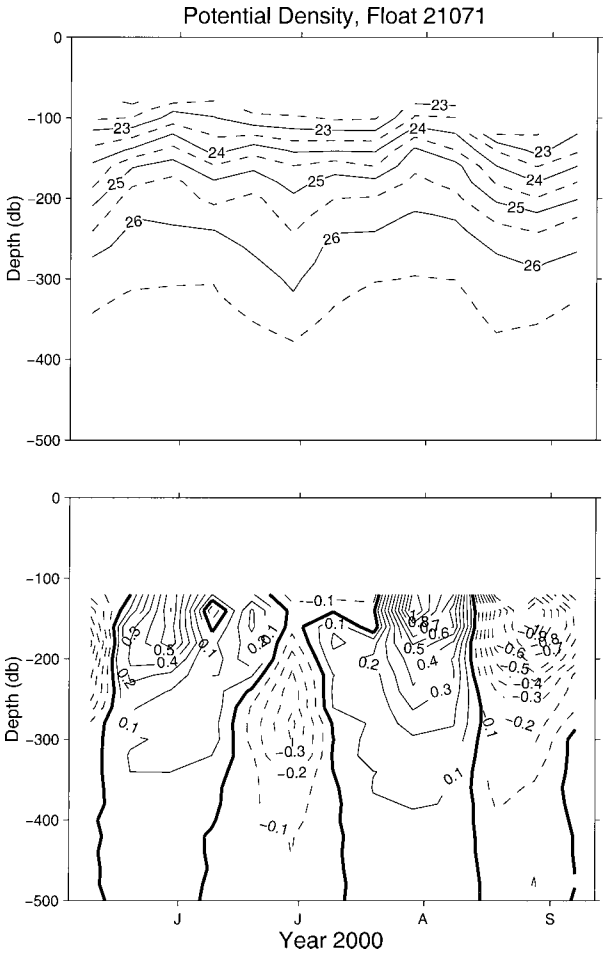


FIG. 12. Time series of potential density $\sigma_\theta$ (upper panel) and its anomaly (lower-panel) from measurements of PALACE float (21071) at 11°–12°S, 109°E in the SEC region. The unit is kg m$^{-3}$.

wave's amplitude and phase (Fig. 13). The density anomaly calculated from the linear instability solution shows a subsurface density anomaly maximum similar to that determined from the WOCE section and float data (Fig. 13a). The amplitude from the linear model has been scaled to have a surface velocity magnitude of of 44 cm s$^{-1}$, corresponding to a sea level amplitude of 12 cm. The depth of maximum amplitude of the perturbations are slightly different between the observations (100–150 m) and model (60 m). We find good correspondence between the observed and predicted wave phase, which increases with depth below 100 m (Fig. 13b). The upward phase propagation in the thermocline denotes the downward propagation of energy.

## 6. Available potential energy budget

Because baroclinic instability draws available potential energy (APE) from the mean flow, we analyze below the APE balance within the SEC. Consider the volume of ocean from 9.5°–13.5°S, 108.5°–114.5°E in the 0–500 m depth range and for the July–September time period:

$$\partial \mathrm{APE}/\partial t + R_{\mathrm{tras}} = C_E(K, P) + \text{advection} + \text{residual}. \quad (1)$$

The first term on the lhs is the temporal change of the mean flow APE, $R_{\mathrm{tras}}$ is the conversion rate of APE from the mean flow to the eddy field due to instability, and $C_E(K, P)$ is the increase in mean flow APE due to local Ekman pumping.

The mean flow APE is defined as (Oort et al. 1994)

$$\mathrm{APE} = -\frac{1}{2}\int_v g(\rho - \overline{\rho})^2(\partial\overline{\rho_\theta}/\partial z)^{-1}\, dV, \quad (2)$$

where $\rho = \rho(x, y, z, t)$ is the sea water density and $\overline{\rho}$ and $\overline{\rho}_\theta$ are the annual mean spatial average density and potential density profile in this region. These are calculated from the monthly temperature and salinity climatology. The peak APE occurs in September, with a value of nearly $2 \times 10^4$ J m$^{-2}$, and there is a steady increase of APE during July–September at an average

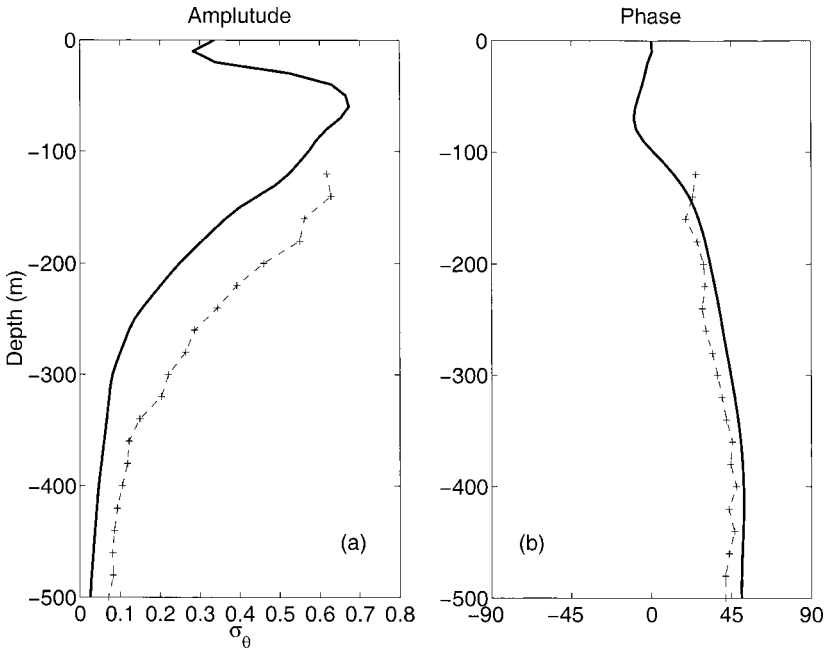


FIG. 13. Vertical distribution of the (a) amplitude and (b) phase of potential density of the most unstable mode at 113.5°E during Jul–Sep when assuming a surface elevation amplitude of 12 cm. The dashed lines are derived from a (60 day) sine wave fit of the PALACE float data.

rate of about 1 mW $m^{-2}$ (Fig. 14a). The advection of APE is evaluated by integrating $\int_S \mathbf{u}$ APE $dS$ along the box boundaries. Only considering the zonal direction, the mean flow advection contributes to an increase in the APE by the magnitude of 2 mW $m^{-2}$ during July–September.

The increase in mean flow APE due to Ekman pumping in the SEC box can be calculated as

$$C_E(K, P) = g \int_v (\rho - \overline{\rho}) w \, dV, \tag{3}$$

where $w$ is the Ekman pumping velocity calculated from the NCEP monthly mean wind stress. Here $C_E(K, P)$ has a peak value of about 1.5 mW $m^{-2}$ in September (Fig. 14). This compares to the subtropical gyres, which are driven by Ekman pumping rates of magnitude 1 mW $m^{-2}$ (Gill et al. 1974; Wunsch 1998). Because the wind stress curl estimated from the NCEP product is likely an underestimate (A. Schiller 1999, personal communication), we adopt the high September rate as the average Ekman pumping rate during the entire July–September season. The surface heat flux contribution estimated from the Southampton Oceanographic Centre climatology (Josey et al. 1996) is destructive and with a magnitude of less than 1 mW $m^{-2}$ during this time period.

Finally, using the vertical profile of the linear wave structure and assuming an average surface elevation magnitude of 9 cm (6.4 cm in terms of standard deviation, close to averages in Figs. 3 and 4), the energy conversion rate from the mean flow APE to the eddy field from the linear model (see appendix) is shown in Fig. 15a. Large energy conversion only takes place in the upper 300 m. The vertical integral of energy conversion between 0–500 m gives $R_{\text{tras}} = 2.4$ mW $m^{-2}$. Thus, in mW $m^{-2}$, we have 1.5 from the Ekman term plus 2 from advection balancing 1 in an observed increase in APE over the season. This leaves roughly 2.5 to be accounted for by the instability, agreeing with the above estimate based on the linear theory.

Although no error estimates are possible for any of the above terms, the magnitudes of the terms suggest that advection associated with the throughflow plays an important role in supplying APE to the SEC and that the instability is important in dissipating this energy.

## 7. Effects on large-scale flow

Using a linear relation between the density and temperature, we approximate the northward heat flux during July–September to be $2.4 \times 10^{13}$ W from 0 to 500 m in a 6° longitudinal span (Fig. 15b). If we use a mean meridional temperature gradient over 0–500 m of $6 \times 10^{-6}$°C $m^{-1}$ (1.5°C over 2° lat from the climatology), the meridional heat flux corresponds to a meridional mixing coefficient of $\kappa = 3 \times 10^3$ $m^2$ $s^{-1}$. From a scale analysis (Visbeck et al. 1997), $\kappa = \alpha f / R^{1/2} l^2$, where $\alpha = 0.015$ is a ''universal'' constant and $l$ is the meridional scale of the baroclinic flow (3–4°). With Ri = 2000, $\kappa = 1$–$2 \times 10^3$ $m^2$ $s^{-1}$, in comparable magnitude with

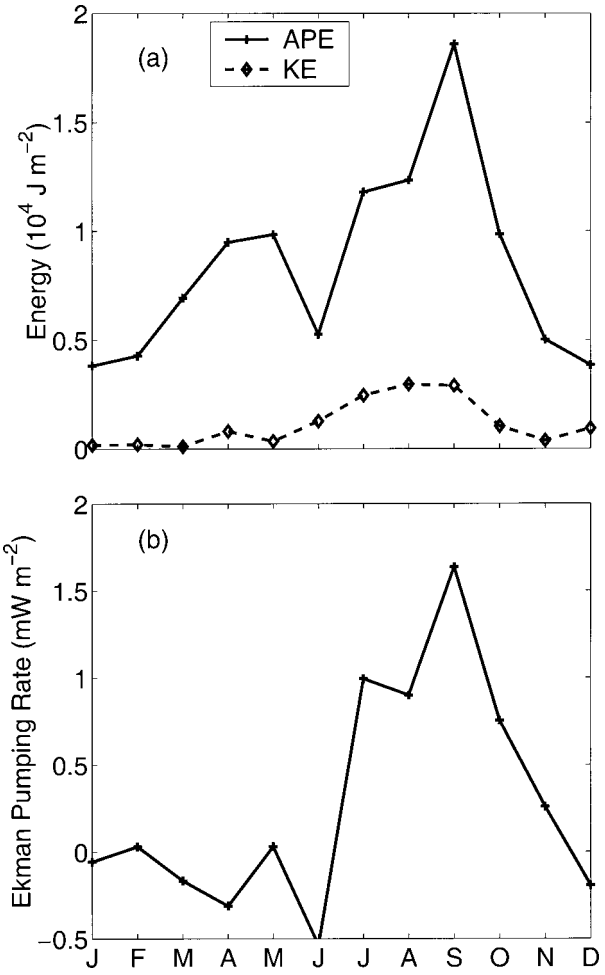


FIG. 14. (a) The temporal variation of mean flow APE and kinetic energy in the SEC and (b) the Ekman pumping rate in the SEC box integrated over 0–500 m based upon the monthly climatology and NCEP data.

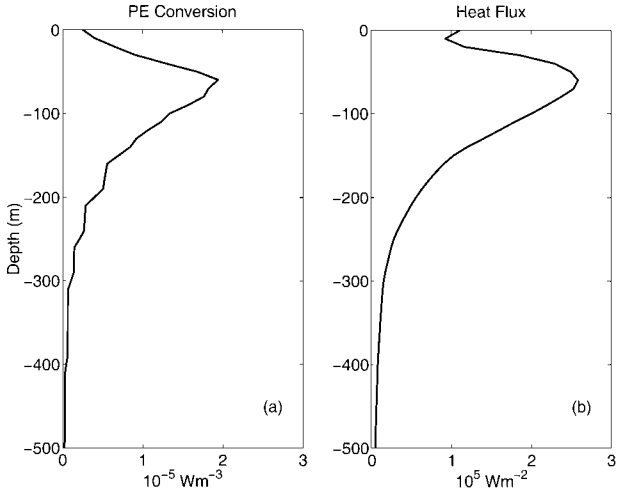


FIG. 15. (a) Energy conversion rate and (b) meridional heat flux for the most unstable mode at 113.5°E during Jul–Sep, assuming an average surface elevation amplitude of 9 cm.

the result from the linear model. Using a simple advection–diffusion model of the throughflow water along an isopycnal, the isopycnal mixing coefficient was estimated to be $1.1 \times 10^4$–$1.6 \times 10^4$ m$^2$ s$^{-1}$ (Gordon et al. 1997). Their overestimation may be due to assuming too large an advection velocity in the SEC.

The northward heat flux above 500 m from the above estimate is comparable with the magnitude of heat flux needed to counter upwelling cooling along the Sumatra–Java coast (Qu et al. 1994). Also the heat flux due to the instability can reduce the vertical temperature gradient near the coastal region and thus could reduce the cooling effect of the wind-driven coastal upwelling.

Masumoto and Meyers (1998) noted that the eastern boundary influence on the annual Rossby wave along 12°S decayed quickly in the region where we find the instability. Thus, the generation of the instability waves, drawing their energy from the mean flow APE during the June–September season as shown in the above section, may play a major role in dissipating the Pacific-forced annual Rossby wave and thus the throughflow dynamic signal in the Indian Ocean.

## 8. Summary

In the present study, gridded satellite altimeter and profiling float data are used to characterize the intraseasonal variability in the South Equatorial Current (SEC) in the east Indian Ocean. Strong intraseasonal signals are found along 12°S during the second half of the year. The length scale of the variability is 100–150 km with a westward phase speed of 15–19 cm s$^{-1}$ and dominant periods between 40–80 days.

A continuously stratified quasigeostrophic model based on climatological data is used to analyze the baroclinic stability of the SEC. The instability waves have large growth rate (with *e*-folding scale of less that 50 days) only during the July–September season, when the SEC and the Pacific to Indian Ocean throughflow are strongest. The characteristics of the derived instability waves are similar to those observed from altimeter, a WOCE hydrographic section, and profiling float data. Seasonal intensification of the upper 200-m ocean geostrophic shear is crucial for the instability development.

An available potential energy analysis shows that the baroclinic instability draws most of its energy from advection of APE via the throughflow's contribution to the SEC, with local Ekman pumping as a secondary source.

The study shows that a linear quasigeostrophic model can be used to detect and quantify the preferred season and locality of baroclinic instability. Combined with altimeter data, this could provide a useful tool to scale the eddy heat flux in the World Ocean.

*Acknowledgments.* This work was supported by a special executive grant from CSIRO, Australia. We thank

Gary Meyers, Trevor McDougall, Andreas Schiller, Mike Spall, James Potemra, Bo Qiu, Akio Ishida, and two anonymous reviewers for helpful suggestions; and Jeff Dunn, Neil White, and Jim Mansbridge for making the ocean climatology, altimeter, and NCEP products easily accessible. Ann Gronell is thanked for processing the PALACE float data. The altimeter products have been produced by the CLS Space Oceanography Division as part of the European Union Environment and Climate project AGORA and DUACS with financial support from the CEO programme and Midi-Pyrenees regional council.

## APPENDIX

### Baroclinic Instability Calculation

The eddy disturbance has a horizontal velocity scale of $U \sim 0.2$ m s$^{-1}$, and horizontal and vertical length scales of $L \sim 2 \times 10^5$ m and $D \sim 3 \times 10^2$ m. The Coriolis coefficient is $f_0 \sim 3 \times 10^{-5}$ s$^{-1}$, and thus we have a Rossby number of Ro $= U/fL \sim 3 \times 10^{-2}$ and $L/r_0 \sim 3 \times 10^{-2}$, where the earth radius $r_0 \sim 6 \times 10^6$ m, the square of the ratio between the length scale and barotropic deformation radius $F = f^2L^2/gD \sim 1 \times 10^{-2}$, and tan $(-12°) \sim 0.2$. Assuming that the friction terms are small, that is, horizontal and vertical Ekman numbers $E_H = 2A_H/fL^2 <$ Ro, $E_V = 2A_V/fD^2 <$ Ro, the disturbance is hydrostatic, $\beta$-plane, quasigeostrophic motion in a Cartesian coordinates (Pedlosky 1987).

Following Gill et al. (1974), we consider small disturbances to a mean state in which the density $\overline{\rho}$ varies with both depth and meridional position. The horizontal scale, $k^{-1}$, of the perturbation is assumed to be small compared with the horizontal scale of the density variations, so that locally the perturbation can be considered to be a superposition of plane wave solutions, and the only properties of the mean field on which the solution depends are the variations of $\overline{\rho}$ and of its meridional gradient. A disturbance streamfunction $\psi$ is introduced, which for a plane wave that satisfies a no-meridional flow condition at $y = \pm L$, has the form (Johns 1988)

$$\psi(x, y, z, t) = \mathrm{Re}[\phi(z) \cos(\pi y/2L) \exp ik(x - ct)].$$

so that

$$p = \rho_0 f\psi, \qquad u = -\psi_y, \qquad v = \psi_x,$$

$$g\sigma = -\rho_0 f\psi_z, \qquad N^2 w = -f(\psi_{zt} + \overline{U}\psi_{zx} - \overline{U}_z\psi_x).$$

The equation satisfied by the complex amplitude, $\phi$, of the streamfunction is

$$(\overline{U} - c)\{[(f^2/N^2)\phi_z]_z - (\pi^2/4L^2 + k^2)\phi\} + Q_y\phi = 0,$$

where $Q_y = \beta - \overline{U}_{yy} - [(f^2/N^2)\overline{U}_z]_z$, $f\overline{U}_z = g\overline{\rho}_y/\rho_0$, and $N^2 = -g\overline{\rho}_z/\rho_0$. $\overline{U}_{yy} = -\overline{U}/\delta^2$, where $\delta$ is the half-width of a parabolic jet, with $\overline{U} = 0$ at $y = \pm\delta$. The boundary conditions are $\phi_z/\phi = \overline{U}_z/(\overline{U} - c)$ at sea surface $z = 0$ and sea bottom $z = -H$.

The $N^2$ field is calculated from the temperature and salinity climatology, averaged between 10.5–12.5°S to represent the SEC, and $L \sim \delta \sim 2°$ latitude. The standard depth data are linearly interpolated onto 10-m intervals. The zonal velocity of the SEC, $\overline{U}$, is calculated geostrophically between the two latitudes referenced to 1500 m. According to Johns (1988), $-\partial[(f^2/N^2)\overline{U}_z]/\partial z$ is replaced by $-\partial[f(\partial z/\partial y)_\rho]/\partial z$ in the calculation of $Q_y$. For a given wavenumber $k$, the equations and boundary conditions define an eigenvalue problem for $c$ and are solved using a shooting method. A complex $c$ with a positive imaginary part implies positive growth rate, $c_i k$, and the mean flow is then said to be baroclinically unstable. Twelve initial guesses of $c$ are taken from the semicircle of the unstable waves (Pedlosky 1987) for the eigenvalue problem, and the resultant most unstable wave (maximum growth rate) within the semicircle is used in the analysis.

The energy density of the perturbation is given by

$$E = \frac{1}{2}\rho_0(\psi_x^2 + \psi_y^2 + f^2\psi_z^2/N^2).$$

Expressing $\phi$ in terms of amplitude and phase:

$$\phi(z) = A(z) \exp i\theta(z),$$

then

$$\psi = A(z) \cos(\pi y/2L) \exp(kc_i t) \cos[k(x - c_r t) + \theta(z)],$$

where $A(z)$ is normalized to 1 at sea surface. The zonally averaged energy transfer rate from the mean flow APE to the perturbation field is

$$R_{\mathrm{trans}} = \frac{1}{4}\rho_0 k^{-1} \int_{-H}^{0} \left(\frac{f}{N}\right)^2 \overline{U}_z\theta_z v^2(0)\, dz,$$

and the corresponding meridional heat transport, by assuming a linear relationship between potential density and temperature is

$$H_{\mathrm{trans}} = \frac{1}{4}\rho_0 \int_{-H}^{0} \left(\frac{c_p f\theta_z}{\alpha_T g k}\right) v^2(0)\, dz,$$

where $v(0)$ is the average sea surface velocity amplitude, $c_p$ is the specific heat of sea water, and $\alpha_T$ is the thermal expansion coefficient.

## REFERENCES

Arief, D., and S. P. Murray, 1996: Low-frequency fluctuations of the Indonesian throughflow through Lombok Strait. *J. Geophys. Res.,* **101,** 12 455–12 464.

Bray, N. A., S. E. Wijffels, J. C. Chong, M. Fieux, S. Hautala, G. Meyers, and W. M. L. Morawitz, 1997: Characteristics of the Indo-Pacific throughflow in the eastern Indian Ocean. *Geophys. Res. Lett.,* **24,** 2569–2572.

Broecker, W. S., 1991: The great ocean conveyor. *Oceanography*, **4** (2), 79–89.

Chong, J. C., J. Sprintall, S. Hautala, W. L. Morawitz, N. A. Bray, and W. Pandoe, 2000: Shallow throughflow variability in the outflow straits of Indonesia. *Geophys. Res. Lett.,* **27** (1), 125–128.

Feng, M., G. Meyers, and S. Wijffels, 2001: Interannual upper ocean variability in the tropical Indian Ocean. *Geophys. Res. Lett.*, in press.
Gill, A. E., 1982: *Atmosphere–Ocean Dynamics.* Academic Press, 662 pp.
——, J. S. A. Green, and A. J. Simmons, 1974: Energy partition in the large-scale ocean circulation and the production of mid-ocean eddies. *Deep-Sea Res.*, **21,** 499–528.
Godfrey, J. S., 1996: The effect of the Indonesian throughflow on ocean circulation and heat exchange with the atmosphere: A review. *J. Geophys. Res.*, **101,** 12 217–12 237.
Gordon, A. L., 1986: Interocean exchange of thermocline water. *J. Geophys. Res.*, **91** (C4), 5037–5047.
——, S. Ma, D. B. Olson, P. Hacker, A. Field, L. D. Talley, D. Wilson, and M. Baringer, 1997: Advection and diffusion of Indonesian throughflow water within the Indian Ocean South Equatorial Current. *Geophys. Res. Lett.*, **24** (21), 2573–2576.
Hirst, A. C., and J. S. Godfrey, 1993: The role of the Indonesian Throughflow in a global ocean GCM. *J. Phys. Oceanogr.*, **23,** 1057–1086.
Johns, W. E., 1988: One-dimensional baroclinically unstable waves on the Gulf Stream potential vorticity gradient near Cape Hatteras. *Dyn. Atmos. Oceans*, **11,** 323–350.
Josey, S. A., E. C. Kent, D. Oakley, and P. K. Taylor, 1996: A new global air–sea heat and momentum flux climatology. *Int. WOCE Newsl.*, **24,** 3–5.
Kashino, Y., H. Watanabe, B. Herunadi, M. Aoyama, and D. Hartoyo, 1999: Current variability at the Pacific entrance of the Indonesian throughflow. *J. Geophys. Res.*, **104,** 11 021–11 035.
Lau, K.-M., and H. Weng, 1995: Climate signal detection using wavelet transform: How to make a time series sing. *Bull. Amer. Meteor. Soc.*, **76,** 2391–2402.
Le Traon, P. Y., F. Nadal, and N. Ducet, 1998: An improved mapping method of multi-satellite altimeter data. *J. Atmos. Oceanic Technol.*, **25,** 522–534.
Levitus, S., and T. P. Boyer, 1994: *World Ocean Atlas 1994.* Vol. 4: *Temperature*, NOAA Atlas NESDIS 4, 117 pp.
——, R. Burgett, and T. P. Boyer, 1994: *World Ocean Atlas 1994.* Vol. 3: *Salinity*, NOAA Atlas NESDIS 3, 99 pp.
Lukas, R., T. Yamagata, and J. P. McCreary, 1996: Pacific low-latitude western boundary currents and the Indonesian throughflow. *J. Geophys. Res.*, **101,** 12 209–12 216.
Madden, R. A., and P. R. Julian, 1994: Observations of the 40–50 day tropical oscillation—A review. *Mon. Wea. Rev.*, **122,** 814–837.
Masumoto, Y., and G. Meyers, 1998: Forced Rossby waves in the southern tropical Indian Ocean. *J. Geophys. Res.*, **103,** 27 589–27 602.
Meehl, G. A., 1993: A coupled air–sea mechanism in the tropical Indian Ocean and Pacific regions: Role of the ocean. *J. Climate*, **6,** 31–41.
Meyers, G., R. J. Bailey, and A. P. Worby, 1995: Geostrophic transport of the Indonesian throughflow. *Deep-Sea Res.*, **42,** 1163–1174.
Molcard, R., M. Fieux, J. C. Swallow, A. G. Ilahude, and J. Banjarnahor, 1994: Low frequency variability of the currents in Indonesian Channels (Savu-Roti and Roti-Ashmore Reef). *Deep-Sea Res.*, **41,** 1643–1662.
——, ——, and A. G. Ilahude, 1996: The Indo–Pacific throughflow in the Timor Passage. *J. Geophys. Res.*, **101,** 12 411–12 420.
Murtugudde, R., A. J. Busalacchi, and J. Beauchamp, 1998: Seasonal-to-interannual effects of the Indonesian throughflow on the tropical Indo–Pacific Basin. *J. Geophys. Res.*, **103,** 21 425–21 441.
Nicholls, N., 1989: Sea surface temperatures and Australian winter rainfall. *J. Climate*, **2,** 965–973.
Oort, A. H., L. A. Anderson, and J. P. Peixoto, 1994: Estimates of the energy cycle of the oceans. *J. Geophys. Res.*, **99,** 7665–7688.
Pedlosky, J., 1987: *Geophysical Fluid Dynamics.* Sprinter-Verlag, 624 pp.
Philander, S. G. H., 1978: Instabilities of zonal equatorial currents, 2. *J. Geophys. Res.*, **83,** 3679–3682.
Ponte, R. M., and D. S. Gutzler, 1992: 40–60 day oscillations in the western tropical Pacific: Results from an eddy-resolving global ocean model. *Geophys. Res. Lett.*, **19,** 1475–1478.
Potemra, J., 1999: Seasonal variations of upper ocean transport from the Pacific to the Indian Ocean via Indonesian straits. *J. Phys. Oceanogr.*, **29,** 2930–2944.
Qiu, B., M. Mao, and Y. Kashino, 1999: Intraseasonal variability in the Indo–Pacific Throughflow and the regions surrounding the Indonesian seas. *J. Phys. Oceanogr.*, **29,** 1599–1618.
Qu, T., G. Meyers, J. S. Godfrey, and D. Hu, 1994: Ocean dynamics in the region between Australia and Indonesia and its influence on the variation of sea surface temperature in a global GCM. *J. Geophys. Res.*, **99,** 18 433–18 445.
Quadfasel, D., and G. R. Cresswell, 1992: A note on the seasonal variability of the South Java Current. *J. Geophys. Res.*, **97,** 3685–3688.
——, A. Frische, and G. Cresswell, 1996: The circulation in the source area of the South Equatorial Current in the eastern Indian Ocean. *J. Geophys. Res.*, **101,** 12 483–12 488.
Ripa, P., 1991: General stability conditions for a multi-layer model. *J. Fluid Mech.*, **222,** 119–137.
Schiller, A., J. S. Godfrey, P. C. McIntosh, G. Meyers, and S. E. Wijffels, 1998: Seasonal near-surface dynamics and thermodynamics of the Indian Ocean and Indonesian Throughflow in a global ocean general circulation model. *J. Phys. Oceanogr.*, **28,** 2288–2312.
Schneider, N., and T. P. Barnett, 1997: Indonesian throughflow in a coupled general circulation model. *J. Geophys. Res.*, **102,** 12 341–12 358.
Semtner, A. J., and R. M. Chervin, 1992: Ocean general circulation from a global eddy-resolving model. *J. Geophys. Res.*, **97,** 5493–5550.
Sprintall, J., J. C. Chong, F. Syamsudin, W. Morawitz, S. Hautala, N. Bray, and S. Wijffels, 1999: Dynamics of the South Java Current in the Indo-Australian Basin. *Geophys. Res. Lett.* **26,** 2493–2496.
——, A. L. Gordon, R. Murtugudde, and R. D. Susanto, 2000: A semiannual Indian Ocean forced Kelvin wave observed in the Indonesian seas in May 1997. *J. Geophys. Res.*, **105,** 17 217–17 230.
Stammer, D., 1997: Global characteristics of ocean variability estimated from regional TOPEX/Poseidon altimeter measurements. *J. Phys. Oceanogr.*, **27,** 1743–1769.
——, 1998: On eddy characteristics, eddy transports, and mean flow properties. *J. Phys. Oceanogr.*, **28,** 727–739.
Susanto, R. D., A. L. Gordon, J. Sprintall, and B. Herunadi, 2000: Intraseasonal variability and tides in Macassar Strait. *Geophys. Res. Lett.*, **27,** 1499–1502.
Tomczak, M., and J. S. Godfrey, 1994: *Regional Oceanography: An Introduction.* Pergamon, 422 pp.
Visbeck, M., J. Marshall, T. Haine, and M. Spall, 1997: Specification of eddy transfer coefficients in coarse-resolution ocean circulation models. *J. Phys. Oceanogr.*, **27,** 381–402.
Watanabe, H., and Coauthors, 1997: Moored measurement of the Indonesian throughflow at the southwestern edge of the Philippine Sea. *Int. WOCE Newsl.*, **27,** 26–30.
Webster, P. J., A. Moore, J. Loschnigg, and M. Leban, 1999: Coupled ocean–atmosphere dynamics in the Indian Ocean during 1997–1998. *Nature.*, **40,** 356–360.
Wijffels, S. E., N. A. Bray, S. Hautala, G. Meyers, and W. M. L. Morawitz, 1996: The WOCE Indonesian throughflow repeat hydrography sections: I10 and IR6. *Int. WOCE Newsl.*, **24,** 25–28.
——, J. Sprintall, M. Fieux, and N. Bray, 2001: The throughflow in the southeast Indian Ocean. Part I: Water mass variability. *Deep-Sea Res.*, in press.
Wunsch, C., 1998: The work done by the wind on the oceanic general circulation. *J. Phys. Oceanogr.*, **28,** 2332–2340.
——, 1999: Where do ocean eddy heat fluxes matter? *J. Geophys. Res.*, **104,** 13 235–13 249.